

# Development and Application of the SparkJet Actuator for High-Speed Flow Control

*Sarah H. Popkin, Trent M. Taylor, and Bohdan Z. Cybyk*

**A**ctive flow control, a field dedicated to developing techniques to improve vehicle performance characteristics through local flow manipulation, has successfully generated several devices capable of controlling low-speed, subsonic flows. However, the availability of analogous devices or techniques for high-speed, supersonic flows is limited. A promising plasmadynamic device, the SparkJet actuator, is being developed at APL under Air Force Office of Scientific Research sponsorship. In collaboration with Florida State University and the Air Force Research Laboratory, priority applications will include, but are not limited to, mitigating unsteady pressure waves in open supersonic bomb bay cavities and reducing flow separation on low-pressure turbine blades to improve turbojet efficiency. After an introduction to targeted applications for the SparkJet, this article will describe the experimental and numerical modeling techniques, including recent supersonic wind tunnel tests, used to evaluate SparkJet performance, the conclusions drawn from these techniques, and the challenges associated with evaluating SparkJet performance.

## INTRODUCTION

In the last 20 years, attention within the aerospace community has turned to the field of active flow control (AFC) because of success in controlling adverse aerodynamic conditions that affect vehicle performance with AFC. AFC methods have emerged as one of the enabling technologies that can be beneficial for a wide range of internal and external flows for the next generation of

military and civilian aircraft. AFC, unlike passive flow control, can be selectively activated when flow conditions can be improved yet offer no aerodynamic (drag) penalty when not in operation. AFC works by using devices that introduce energy into a layer of air enveloping a surface. This layer of air, called the boundary layer, develops because of friction between the air and

vehicle surface and results in a loss of kinetic energy and momentum. Ideally, the introduction of energy from an AFC device occurs in a way that significantly influences the boundary layer to improve the flow environment on the surface and around the flight vehicle. Performance benefits include, but are not limited to, reducing drag, improving control surface (e.g., aileron, flap, rudder, and elevator) effectiveness, replacing control surfaces, controlling unsteady flow effects, and improving fuel mixing. AFC devices intended for low-speed applications (<100 m/s) have been successfully demonstrated and include synthetic jets produced by flexible membranes,<sup>1</sup> dielectric barrier discharge plasma actuators,<sup>2</sup> microelectromechanical systems, mass injection systems, and control surfaces.<sup>3,4</sup> Figure 1 shows examples of how a synthetic jet and a plasma actuator can introduce momentum into the boundary layer. In these diagrams, the synthetic jet actuator introduced momentum to the boundary layer normal to the surface, whereas the dielectric barrier discharge plasma actuators introduce momentum tangential to the surface. Low-speed AFC devices have been well characterized and demonstrated for effectiveness. However, devices and techniques applicable to high-speed flows, including supersonic and hypersonic flows, are limited and continue to be an area of active research.

Only a few AFC devices, including steady microjets, localized arc filament plasma actuators, and pulse detonation actuators, have been experimentally tested in high-speed (supersonic) flows. In the case of fluidic-based steady microjets, experimental testing has demonstrated the efficacy of flow control using steady microjet arrays for a number of applications.<sup>5-8</sup> These applications range from separation control and lift enhancement—where large separated flows were reattached—to the control of flow unsteadiness and/or substantial noise reduction in supersonic impinging jets and cavity flows. Although the effect of steady microjet control has been significant in most applications, research has also demonstrated that pulsing the jets (i.e., unsteady operation)

would produce further enhancements. Unsteady operation can be used to delay flow separation because it can promote mixing in the boundary layer by pulsing at frequencies that match natural instabilities in the flow. Unsteady operation can also be used to introduce oscillations into the flow that interrupt the formation of undesired instabilities, which in turn can delay transition from laminar flow to turbulent flow.

To truly realize the potential of unsteady actuation, and for flow control to become practical, the actuators must perform at frequencies that are inherent in the base flows in order to take advantage of the flow instabilities/time scales. For most high-speed flow applications, this translates to a need for actuation in the kilohertz range, where the actuators must produce both a high mean as well as unsteady output over a large dynamic range. Most existing unsteady actuators do not meet these requirements; they either provide unsteady actuation with relatively low amplitudes—generally over a small range of frequencies—or produce high-amplitude outputs that are either steady or can only be modulated at low frequencies. Almost a decade ago, under independent research and development funding, APL invented the SparkJet actuator<sup>9</sup> specifically for high-speed applications with the desired capability of providing a high-speed pulsating jet with large bandwidth. Under AFOSR (Air Force Office of Scientific Research) sponsorship since 2006, APL has experimentally and numerically studied the SparkJet actuator. The supersonic AFC potential of the SparkJet actuator has led other research groups to test the effectiveness of SparkJet-like actuators.<sup>10,11</sup> This article provides a summary of the AFOSR-sponsored SparkJet technology development, including the methods used to characterize the SparkJet and the drive to experimentally demonstrate actuator arrays in supersonic flow streams.

## APPLICATIONS

The two priority applications for the SparkJet actuator are (i) supersonic flow control over a cavity such as an open weapons bay or landing gear cavity and (ii) flow separation control over wings and/or a fuselage. In open cavity flow problems, the boundary layer develops over the front of the aircraft, thickening until it reaches the open cavity. The boundary layer then detaches from the aircraft surface, becoming what is called a shear layer, and impinges on the back wall of the cavity. The impinging causes acoustic reflections back into the cavity which then cause the

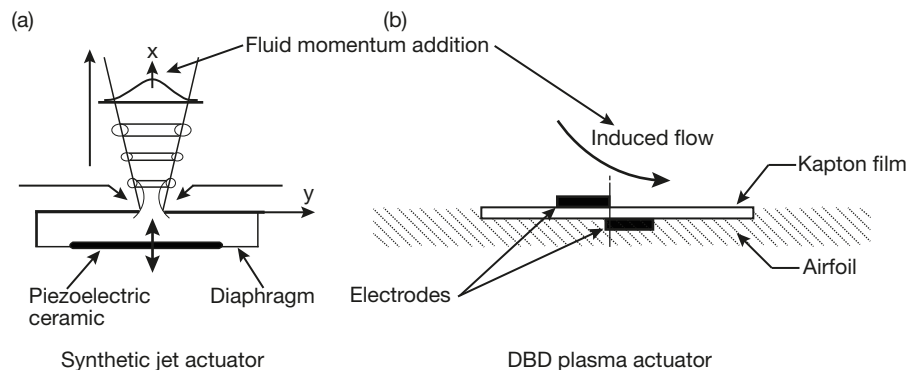


**Figure 1.** Schematic of a synthetic jet actuator (a) and a plasma actuator (b), including the direction of the net fluid momentum addition. DBD, dielectric barrier discharge. (Panel a reproduced with permission from Ref. 1; panel b reproduced with permission from Ref. 2.)

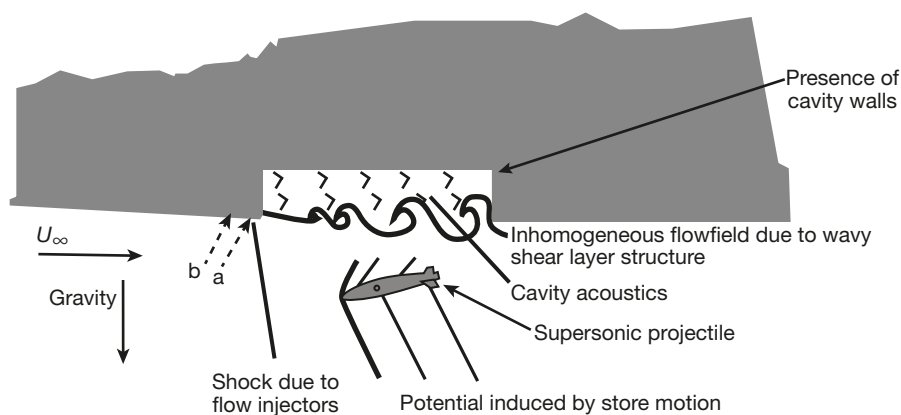


**Figure 2.** Factors affecting the trajectory of the released store under supersonic cross flow and in the presence of microjet-based actuators (locations indicated by a and b).  $U$ , velocity (m/s). (Reproduced with permission from Ref. 6.)

shear layer to oscillate, creating unsteady pressure oscillations inside and near the cavity. These effects are shown in Fig. 2. In the case of releasing a store from the cavity, the unsteady oscillations result in unpredictable store separation; the store may fly back toward the aircraft, potentially damaging the aircraft. At subsonic speeds, spoilers are used to ensure safe store separation. However, at supersonic speeds, the spoilers are less effective. Hence, research has turned to the development and application of high-energy AFC devices.

HIFEX (High Frequency Excitation), a Defense Advanced Research Projects Agency (DARPA)-funded project, included a successful sled test at the High-Speed Test Track at the Holloman Air Force Base in New Mexico. At this test, a cavity was accelerated to Mach 1.77 and microjets were used to control the problematic, unsteady pressure oscillations such that a store was ejected safely through the shear layer and away from the sled.<sup>12</sup> This test used two rows of 150 microjets at, and slightly forward of, the cavity leading edge, with the strength of the jets determined from wind-tunnel testing earlier in the HIFEX program. Although the AFC tech-

nique used in this test used steady jets and proved successful, other AFC research suggests that unsteady actuation can be more effective because it can take advantage of unsteadiness in the flow environment and specifically target the oscillations to “break up” the unsteadiness. With this idea in mind, SparkJet actuator arrays are a promising candidate to provide high-energy, unsteady airjets targeted to mitigate cavity pressure oscillations.

The notion that SparkJet actuators can influence high-speed, even supersonic,

flows arose from numerical simulations. Using a time-accurate, 3-D Reynolds-averaged Navier–Stokes computational fluid dynamics (CFD) flow solver, a simulation of a single SparkJet actuator firing into a Mach 3 cross flow over a flat plate showed that the jet plume penetrates the boundary layer.<sup>13</sup> Figure 3 presents a snapshot of predicted Mach number contours along the symmetry plane 30  $\mu$ s after initiating a single SparkJet device. The contour levels were chosen to show only the details within the boundary layer. The turbulent Mach 3 stream flows from left to right over the flat plate. Visible in this figure are the complex flow field that is formed when the hot gas is expelled out of the device and the successful penetration of the fully developed turbulent boundary layer. Very recently, boundary layer penetration of the SparkJet in a Mach 1.5 crossflow has been experimentally accomplished, thereby supporting the potential proposed by previous computational simulations.<sup>14</sup>

The second priority application—flow separation control—has many practical applications in both external flows, such as over airfoils (aircraft wings, turbine and compressor blades), and internal flows, such as

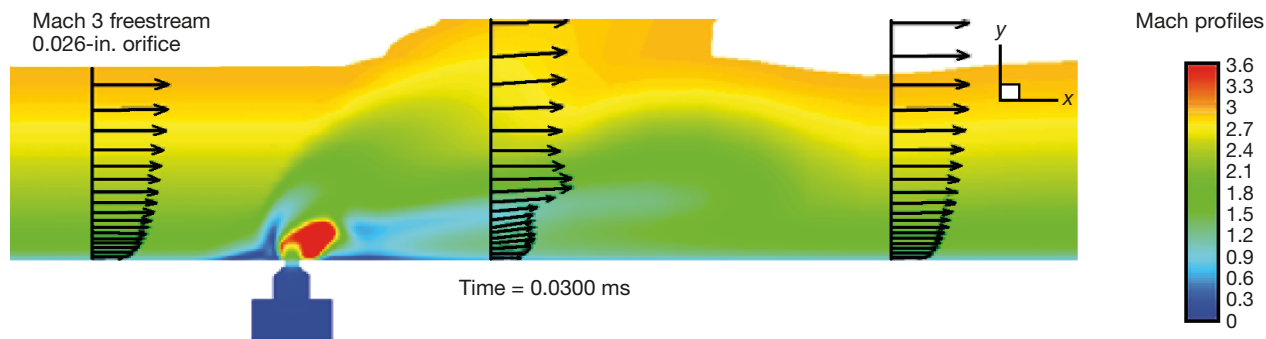


**Figure 3.** Mach contours of the interaction between a SparkJet and a Mach 3 freestream, with vectors of velocity magnitude. (Reproduced from Ref. 13 with permission of the American Institute of Aeronautics and Astronautics.)

diffuser/inlet ducts and pipes. Flow separation occurs when the friction between the air and the flow surface reduces the kinetic energy in the flow enough that the flow near the surface reverses and starts to move upstream. When this happens, the aerodynamic surface geometry effectively changes, adversely affecting vehicle performance efficiency. In a study primarily sponsored by NASA, Florida State University (FSU) used strategically placed actuators to completely reattach the flow and energize the boundary layer.<sup>5</sup> The efficacy of this technique was examined for

managing flow behavior using an adverse pressure gradient ramp, which is shown in Fig. 4. The flow on the ramp is representative of flows on the suction side of turbine and compressor blades, where flow separation is likely to occur. Figure 5a shows a representative ensemble-averaged velocity field for flow over this ramp at a freestream velocity of 65 m/s (primary flow is from left to right). As one proceeds downstream in the vicinity of the surface, there is a rapid deceleration in the fluid velocity, eventually leading to a region of reverse flow. This reverse-flow zone corresponds to the area of dark blue velocity contours, indicating that a closed separation bubble with recirculating flow is present. The effect of control is shown in Fig. 5b, where the activation of

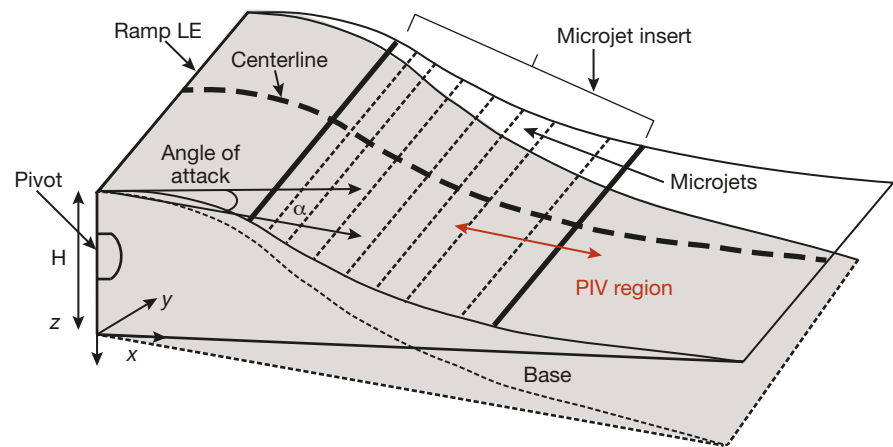


**Figure 4.** Schematic of the test model mounted in the test section to produce a region of separated flow. H, height; LE, leading edge; PIV, particle image velocimetry. (Reproduced with permission from Ref. 5.)

an array of steady (continuous injection) microjets at a very low pressure (and very low mass flow rates) completely eliminates separation. The potential of microarray-based actuators for modifying the flow has been demonstrated in earlier studies using steady microjets.<sup>5</sup> With the ability to create an unsteady jet, the inherent frequencies associated with the external flow can be targeted to produce strong interactions between the jet and external flow to promote mixing of the external, high-kinetic energy flow with the boundary layer where kinetic energy of the flow has decreased and flow separation is likely. Hence, it is anticipated that the pulsating, high-throughput SparkJet actuators will produce improved results over the steady microjets.

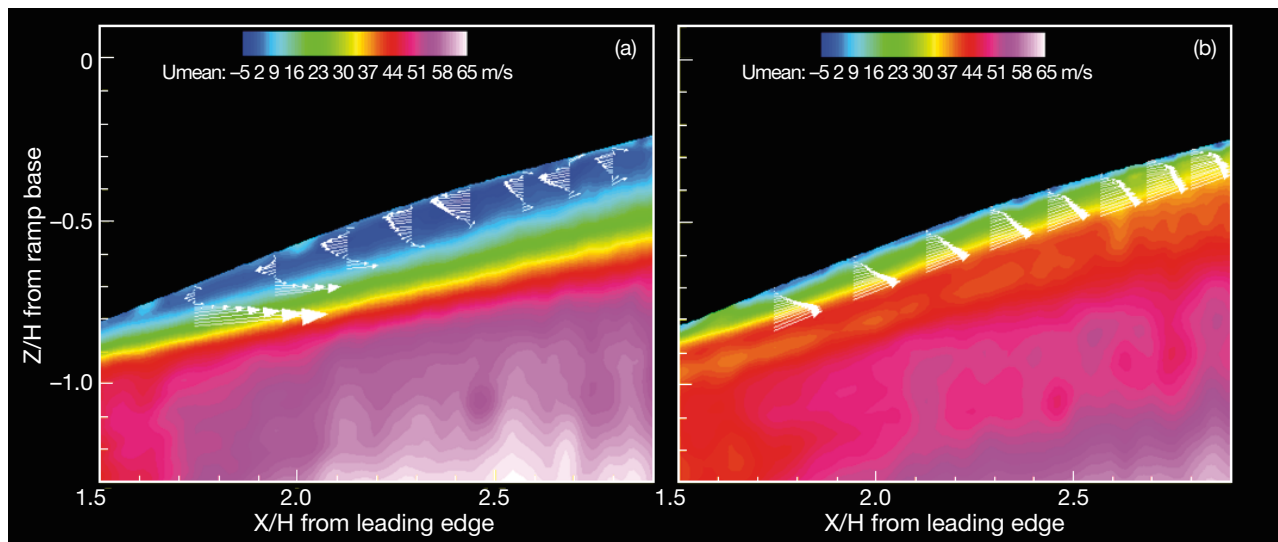


**Figure 5.** Streamwise velocity contour and vectors at  $U_\infty = 65$  m/s (incoming flow from left), where separated flow is present as indicated by the dark blue region. (a) No control. (b) Control using microjets, upstream of the separated flow region (location not in image). (Reproduced with permission from Ref. 5.)

Effectively controlling the flows within the applications just described requires matching the output from a SparkJet array to the external flow characteristics. For a single SparkJet device, several design parameters can be tuned to effectively influence the particular flow environment. For example, the initial energy deposition can be made stronger, the orifice diameter can be varied, or the actuation frequency can be adjusted. For a SparkJet array, additional parameters can be varied such as orifice spacing, actuation frequency, and injection angle. External flow properties such as velocity, instabilities, and external pressure will determine how the SparkJet design parameters must be adjusted.

This article describes our efforts toward understanding how these parametric variations affect the SparkJet effectiveness. It will summarize the basic concepts behind SparkJet operation and describe the numerical and experimental efforts focused on characterizing the SparkJet.

## SPARKJET TECHNOLOGY

The SparkJet is a solid-state zero-net-mass-flux device that consists of a small chamber or cavity with electrodes and a jet orifice.<sup>13</sup> High chamber pressure is generated by rapidly heating the air inside the SparkJet using an electrical, capacitive arc discharge. The arc discharge is initiated by a high-voltage, low-current trigger spark. The pressure is relieved by exhausting the heated air through an orifice. The SparkJet refreshes itself by drawing in

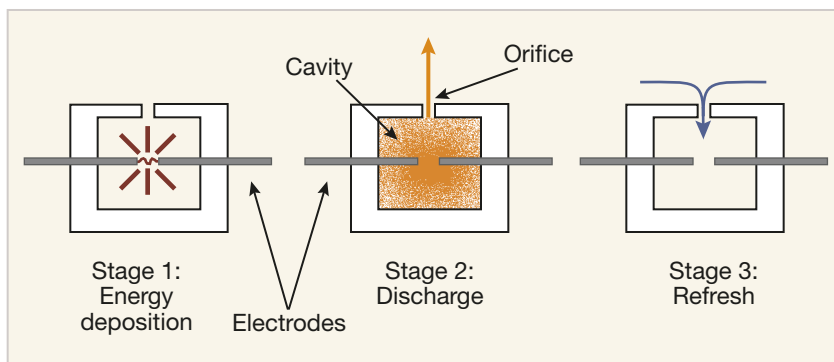


Figure 6. SparkJet cycle.

relatively high-pressure and high-density air. A single cycle of SparkJet operation consists of three distinct stages: energy deposition, discharge, and refresh (Fig. 6).

The actuator design can take on several forms, for example, one spark, one cavity and one orifice or one spark, one cavity, and multiple orifices. The physical size of the orifice and cavity, initial stored capacitive energy, and injection angle of the SparkJet can also be varied. For all practical applications, arrays of SparkJet orifices will be required but the number of orifices per spark and cavity can vary. Figure 7 shows two perspectives of a sample SparkJet array design. This particular design includes a single cavity with a 4- to 400- $\mu\text{m}$ -diameter orifice array.

## CHARACTERIZATION EFFORTS

This section describes the numerical and experimental efforts toward characterizing SparkJet performance. Numerical characterization has involved high-fidelity CFD simulations<sup>16,17</sup> in addition to a simplified simulation based on the numerical solution of ordinary differential equations.<sup>17</sup> The high-fidelity CFD has been used to demonstrate SparkJet temporal and spatial performance in a supersonic cross flow and in quiescent air. In contrast to the high-fidelity CFD results, the simplified numerical modeling provides a temporal-only prediction of the SparkJet performance.

Toward validating the numerical SparkJet models, several experimental techniques have been used to measure SparkJet jet shape, jet velocity and temperature, cavity pressure, and reac-

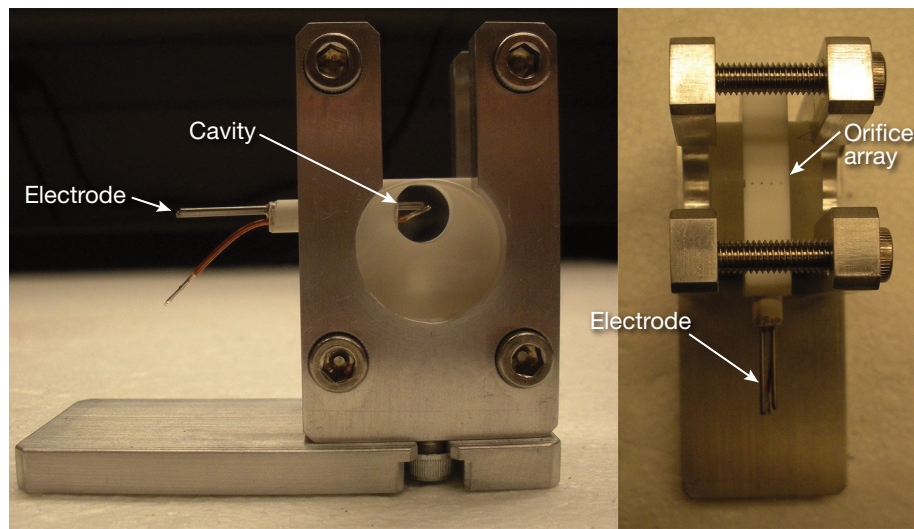


Figure 7. SparkJet array. (Part of this figure reproduced with permission from Ref. 15.)

tion force. Techniques such as Schlieren imaging,<sup>13,18</sup> particle image velocimetry (PIV),<sup>19,20</sup> digital speckle tomography (DST),<sup>19</sup> cavity pressure measurements via a dynamic pressure transducer,<sup>17</sup> and a force stand<sup>20</sup> have been used to acquire these data. Multiple techniques have been used in an attempt to overcome the inherent challenges of measuring dynamic flow conditions within and around such a small device.

### High-Fidelity Modeling

The high-fidelity CFD analyses, primarily for qualitative comparison with experimental results, were performed using the commercial code CFD++ by Metacomp Technologies (<http://www.metacomptech.com>). Although CFD++ is an unstructured code, a fully structured grid created using Gridgen by Pointwise (<http://www.pointwise.com/gridgen/>) was used in the simulations. The majority of the CFD analysis involved a SparkJet firing into quiescent flow. Two primary SparkJet designs have been analyzed using CFD++: single cavity, single orifice and single cavity, four orifices.

For the single-orifice, single-cavity SparkJet design, CFD++ was run axisymmetric and second-order accu-

rate in time and space with a substepping method for time advancement using a thermally perfect single air species with a time step of 5 ns. Figure 8a shows a zoomed view of the grid in the SparkJet chamber. The external grid extended 0.053 m in the expulsion direction (right side of Fig. 8a) and 0.02 m in the radial-flow direction (top of Fig. 8a). It was found that the outer boundary began to influence the solution of the SparkJet after approximately 350  $\mu$ s. Therefore, for longer-duration simulations conducted for 1900  $\mu$ s to investigate the refresh cycle, the grid was extended to 0.35 m and 0.1 m in the expulsion and radial directions, respectively, and the total size of the grid was approximately 149,000 cells. Because the purpose of the CFD simulations was to facilitate a qualitative comparison with experimental results, a grid resolution study was not deemed necessary. Engineering judgment and runtime constraints determined how the grids were created. The red section of the grid in Fig. 8a, representing 65% of the cavity volume, was created as a separate group so that it could be initialized separately from the rest of the flow field. Axisymmetric calculation of the solution, as opposed to a full 3-D calculation, allows for a high grid density without requiring

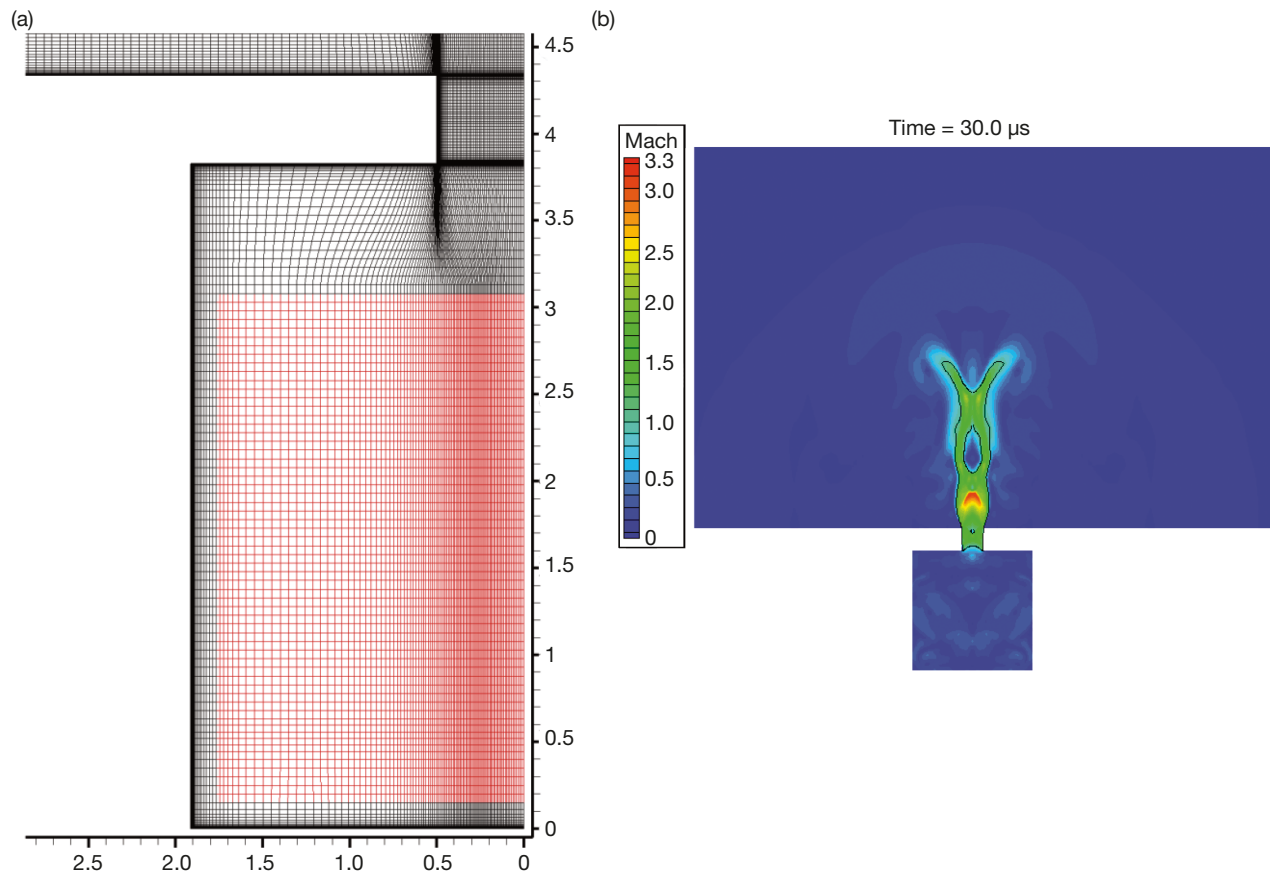


**Figure 8.** (a) Structured axisymmetric grid of a single SparkJet with grid axis units in millimeters. Heated volume shown in red. (b) CFD modeling of the Mach contours in a single SparkJet operating in quiescent flow 30  $\mu$ s after Stage 1 initiation. (Panel a reproduced from Ref. 17 with permission of the American Institute of Aeronautics and Astronautics.)

an unacceptable computation time. The remaining cavity flow and the external flow were initialized at rest and at 288 K and 10,1325 Pa. The red section of the grid was kept at the same density and at rest but was increased in pressure and temperature to model the discharge phase of the SparkJet. The solution was then run time-accurate from there. An example of the Mach contours in the SparkJet operating in quiescent flow is shown in Fig. 8b.

Simulations of the SparkJet array were also conducted using CFD++.<sup>18</sup> The geometry of this simulation is highly 3-D. The 3-D grid was created to be unstructured and symmetric about the dashed line in Fig. 9. Resultant simulations were compared with Schlieren images (shown in the *Schlieren Images* section) for qualitative validation. Figure 9 shows the Mach contours of an array of jets firing into quiescent flow. This array is modeled after the built array shown in Fig. 7. The effects due to the presence of the electrodes, represented by the three white spaces in the cavity in Fig. 9, were included in the model. The grid density of this time-accurate simulation is considerably lower than the previously shown axisymmetric case because of the total increased number of grid points needed for a 3-D simulation. Even though the density is lower, these cases required approximately 10 times more computational time/resources to simulate the same real-time increment. This difference in grid density and computing time demonstrates the computational difficulty when modeling a SparkJet array. This challenge is further exacerbated when modeling array interactions with an external flow and limited computing resources available to APL.

### Simplified Numerical Model

To reduce the computational effort of modeling a SparkJet array and external flow, the SparkJet can be represented as a time-dependent boundary condition at each orifice. The following section describes the efforts toward providing an approximate solution for the SparkJet flow out of the orifice; these efforts resulted in a simplified numerical model of a SparkJet operating in

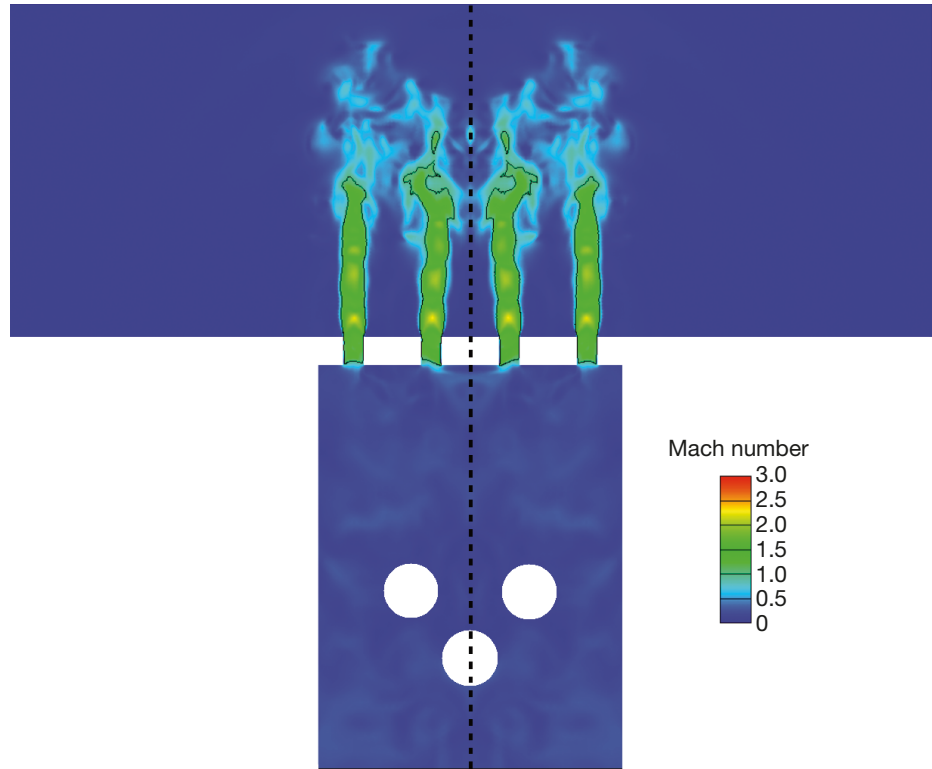


**Figure 9.** CFD modeling of the Mach contours in a SparkJet array operating in quiescent flow 30  $\mu$ s after Stage 1 is initiated.

quiescent flow.<sup>17</sup> This model was created by breaking up the entire SparkJet cycle and modeling the three stages (Fig. 6) separately.

### Stage 1: Energy Deposition

To initiate Stage 1 of the cycle, an instantaneous energy input from the capacitive spark discharge is used to determine the peak temperature ( $T_{peak}$ ) inside the chamber by Eq. 1:

$$T_{peak} = T + \frac{\eta Q}{m C_v}, \quad (1)$$

where  $T$  is the temperature (in Kelvin) just before the spark discharge,  $\eta$  is the efficiency factor,  $Q$  is the stored capacitor energy (in joules),  $m$  is the mass inside the cavity (in kilograms), and  $C_v$  is the specific heat for a constant volume process (in J/kg  $\times$  K).

The total energy stored in the capacitive capacitors is given by Eq. 2:

$$Q = \frac{1}{2} CV^2, \quad (2)$$

where  $C$  is capacitance (in Farads) and  $V$  is the voltage across the capacitors (in volts).

Unfortunately, the energy transferred to heating the air inside the cavity is only a portion of the total capacitive energy. A significant portion of the capacitive

energy goes toward the creation of streamers, molecular ionization, localized heating of the electrodes, and molecular excitation that does not convert to translational energy (heat).<sup>21</sup> This inevitable energy loss leads to a SparkJet efficiency factor,  $\eta$ , applied to this model in Eq. 1. Experimental results presented later in this article will provide information on the actual SparkJet efficiency. Using the ideal gas law [ $P_{\text{peak}} = \rho RT_{\text{peak}}$ , where  $P$  indicates the pressure inside the cavity (in pascals),  $\rho$  is density (in  $\text{kg}/\text{m}^3$ ), and  $R$  is the specific gas constant (in  $\text{J}/\text{kg} \times \text{K}$ )] and under the assumption that no mass leaves the cavity during the instantaneous energy deposition, the peak pressure is also determined and Stage 1 ends.

### Stage 2: Discharge

The peak temperature and pressure from Stage 1 serve as initial conditions for Stage 2; no more energy is added to the system. During Stage 2, the flow is initially choked. The conservation of mass, momentum, and energy equations were manipulated (Eqs. 3–5, respectively) and used to find the changes in cavity density, pressure, and temperature and jet velocity. To eliminate the need for a spatial solution, the cavity and orifice volumes are represented as scalar parameters. To account for the choked and unchoked flow conditions, the exit pressure ( $P_e$ ) boundary conditions were  $P_e = 1.89 P_\infty$  for the choked flow and  $P_e = P_\infty$  for the unchoked flow. Stage 2 ends with high-temperature, low-density, slightly-below-atmospheric-pressure air inside the cavity.

$$\frac{d\rho}{dt} = -\left(\rho A_o \frac{U}{v}\right) \quad (3)$$

$$\frac{dU}{dt} = \frac{1}{\rho} \left( \frac{(p - p_e) A_o - \rho U^2 A_o}{v_o} - U \frac{d\rho}{dt} \right) \quad (4)$$

$$\frac{dT}{dt} = \left( \dot{q} \rho v - (P - P_e) U A_o - \rho \left( C_v T + \frac{U^2}{2} \right) U A_o - v_o \left( 2\rho U \frac{dU}{dt} + U^2 \frac{d\rho}{dt} \right) \right) / \left( C_v v / R \right) \quad (5)$$

### Stage 3: Refresh

During Stage 3, the cavity is refreshed with relatively cool, high-density ambient air because of the slight pressure gradient across the orifice, which is maintained by the continued convective and conductive cooling across the internal cavity surfaces. As the temperatures of the ceramic walls and electrodes drop, the air is also cooled. This maintains a slight pressure gradient until the temperature of the walls reaches the ambient air temperature, at which point the cavity pressure equals ambient pressure. The conservation equations were also used to model this stage by changing the boundary conditions such that the density and temperature of the incoming fluid is that of the external flow. Because Stage 3 is driven by thermodynamic cooling, this process requires further modeling considerations to improve comparisons to CFD during Stage 3.

Figure 10a shows the current model results for the averaged pressure, density, and temperature in the cavity and the velocity of the flow at the orifice. These results compare well to CFD for the same SparkJet configuration ( $Q = 0.091 \text{ J}$ ,  $v = 44 \text{ mm}^3$ ,  $A_o = 0.79 \text{ mm}^2$ ) as modeled in Fig. 10b. When this model is completed, high-frequency actuation can be modeled. During an array design phase, this model will be used to predict the steady-state mass flow rate for a given actuation frequency to determine the SparkJet potential effectiveness when applied to an external flow.

With the ability to model the SparkJet with both high-fidelity and simplified numerical models, design changes can easily be analyzed. However, these models need to be checked against experimental results. Several experimental methods have been used to characterize SparkJet performance, each with limited success. The small

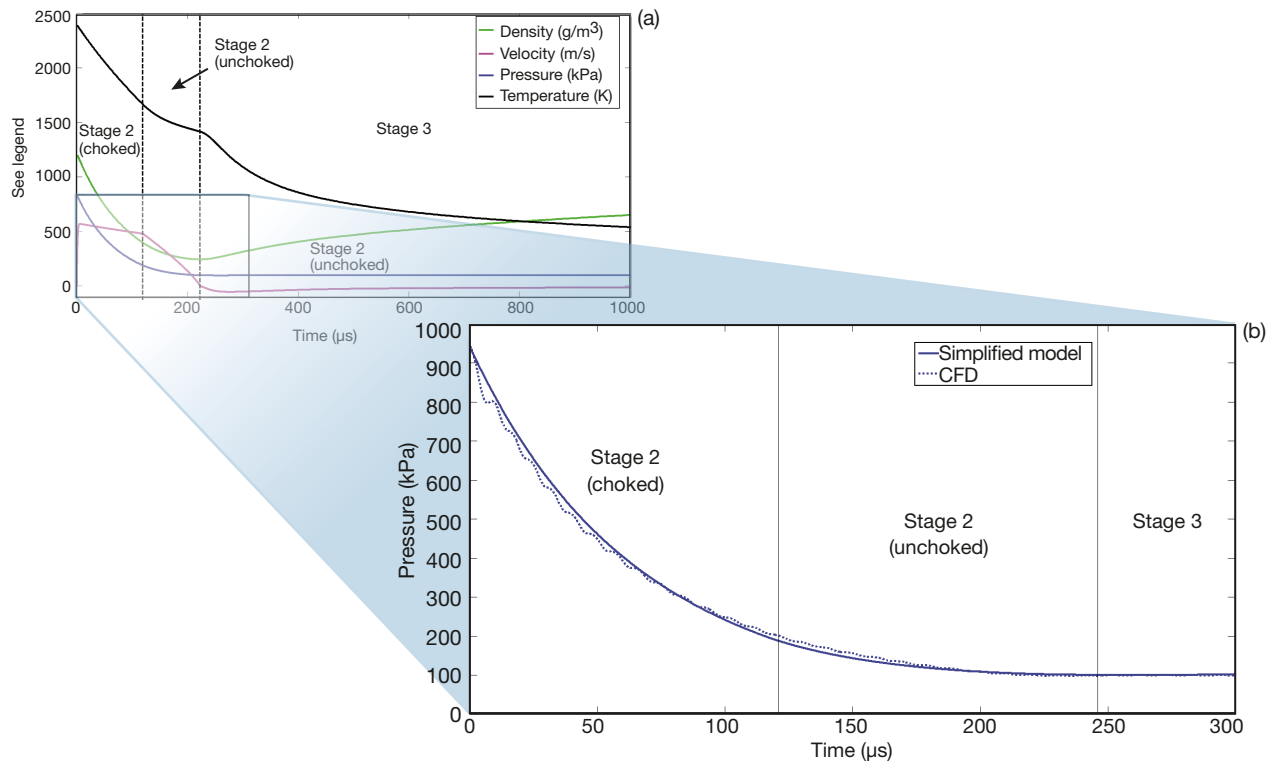


**Figure 10.** Analytical model results showing a time history of the pressure, temperature, density, and orifice velocity during a complete notional SparkJet cycle. (Panel b reproduced from Ref. 17 with permission of the American Institute of Aeronautics and Astronautics.)

size, short cycle duration, large velocity gradients, and strong electromagnetic interference production from the SparkJet actuator push the limits of most experimental techniques and equipment. The following sections describe the multiple experimental efforts and the corresponding results.

### Schlieren Images

The first attempts to qualitatively characterize the SparkJet began with Schlieren images of a single SparkJet firing into quiescent flow.<sup>13</sup> A sparse matrix of experiments with varied chamber volume and orifice diameter has been performed. The resulting high-speed Schlieren images were analyzed to determine initial jet velocity and discharge duration. Frames were filtered using a binary median filter, resulting in well-defined and consistent images of the discharge leading edge. Progression of the leading edge was used to determine jet velocity. A similar approach was used to determine discharge duration. A count of video frames during which flow was attached to the SparkJet orifice was taken, and the camera frame rate was used to determine the discharge duration. Limited temporal resolution precluded accurate quantitative results.

Figure 11 shows a series of Schlieren photographs, separated by 76  $\mu\text{s}$ , illustrating a single discharge from a SparkJet. The design parameters of the SparkJet corresponding to Fig. 11 are given in Table 1. The discharge

from the SparkJet with the larger orifice, shown in Fig. 11, lasts for approximately 0.5 ms.

More recently, as part of the collaborative AFOSR grant with FSU, high-resolution Schlieren images have been acquired in order to estimate the SparkJet performance when designed in an array configuration.<sup>15</sup> Figure 12 shows a comparison between a Schlieren image and CFD simulation of the SparkJet array in operation approximately 30  $\mu\text{s}$  into Stage 2. The flow features in both images share some similarities but not enough for an adequate match. Further work is required to identify the source of the differences.<sup>18</sup> Possible sources include the need to increase grid resolution, the use of a large eddy simulation flow solver rather than a Reynolds-averaged Navier–Stokes solver, or the gradual addition of heat rather than the assumption of instantaneous heat.

### PIV and DST

In order to obtain the quantitative velocity and temperature field measurements needed to characterize the SparkJet discharge, two flow visualization methods are used at The Laboratory for Experimental Fluid Dynamics at the Johns Hopkins University: DST and high-resolution PIV.<sup>19</sup> PIV measures the 2-D velocity gradients of seeded flow regions, and DST measures the 3-D density gradients produced by the SparkJet plume. PIV measurements had been attempted earlier,<sup>20</sup> but there

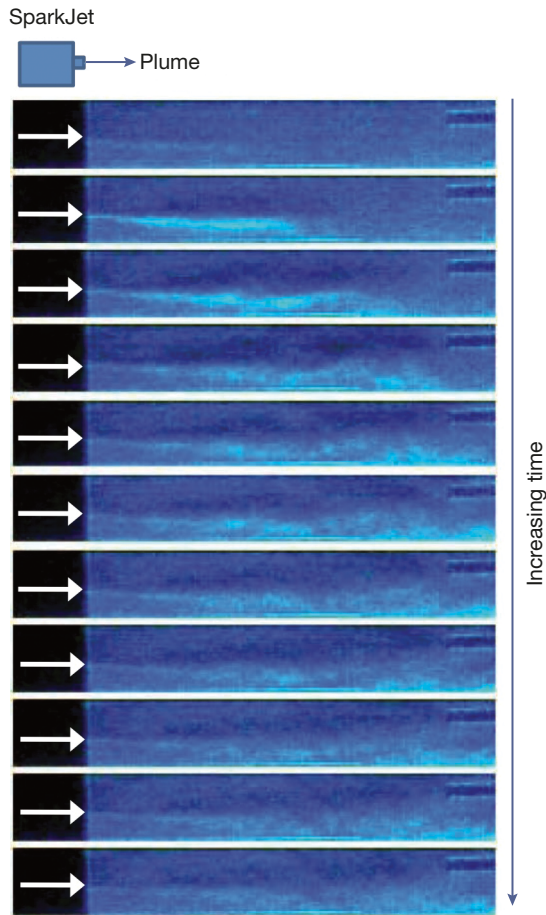


**Figure 11.** Time sequence Schlieren photos, separated by  $76 \mu\text{s}$ , of second-generation discharge from a SparkJet with an orifice diameter of  $0.33 \text{ mm}$ . (Reproduced from Ref. 22 with permission of the American Institute of Aeronautics and Astronautics.)

**Table 1.** SparkJet design parameters corresponding to Fig. 11

Parameter	Value
Orifice diameter	$0.5 \text{ mm}$
Cavity volume	$40.1 \text{ mm}^3$
Discharge energy	$0.02 \text{ J}$

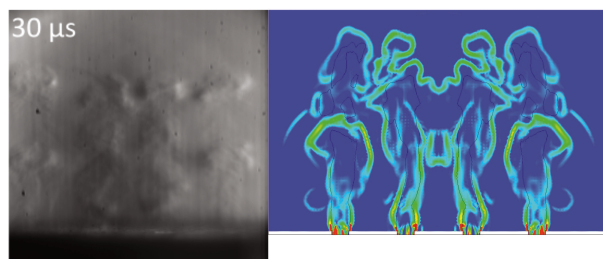


**Figure 12.** Comparison between a Schlieren image and CFD simulation of a SparkJet array in operation  $30 \mu\text{s}$  after firing.

were problems with properly seeding the flow. DST, on the other hand, does not require flow seeding and is a nonintrusive flow-measurement technique. Details on the experimental setup and the specific optical setups for the PIV and DST are available in Ref. 19. The optical equipment and data acquisition system are all synchronized with the trigger for the SparkJet device. There is a delay between the trigger and the imagery equipment to account for the trigger-to-spark discharge event delay. The data processing consists of image enhancement followed by cross-correlation analysis to determine the velocity and density distributions.<sup>23–25</sup>

The SparkJet device tested at the fluid dynamics lab is three times larger than previously used<sup>20</sup> in order to allow more PIV seed particles to enter the cavity and allow better seeding of the flow. The larger SparkJet has an orifice diameter of  $D_{\text{ex}} = 1.0 \text{ mm}$  ( $0.039 \text{ in.}$ ) and a chamber volume  $V_{\text{ch}} = 1.307 \times 10^{-7} \text{ m}^3$ , resulting in an internal energy of the actuator ( $E$ ) of  $0.0342 \text{ J}$ .<sup>22</sup> The capacitor potential to initiate the spark discharge is  $V_i = 600 \text{ V}$ , resulting in an energy deposition ratio,  $Q/E$ , of  $7.414$ , where  $Q$  has been defined in Eq. 2 and  $E$ , the internal energy of the air inside the SparkJet cavity, is defined as  $E = mC_v T$ . The SparkJet was operated at  $1 \text{ Hz}$  to examine the characteristics of a single pulse in quiescent flow.

The resulting flow visualization images acquired show 2-D velocity fields and temperature profiles from PIV and DST measurements, respectively, at various time steps. Figure 13 shows sample results from the PIV and DST. To remain consistent with previous experimental efforts,<sup>20</sup> the PIV results are shown using a colored gradient of the velocity field magnitude (Fig. 11a). In Fig. 11a, the plume velocity magnitude only reaches  $50 \text{ m/s}$ , which is much lower than expected. This lower velocity is probably due to two reasons: first, the efficiency of this SparkJet design was not as high as expected, and second, the terminal velocity of the seed particles is probably near  $50 \text{ m/s}$  and, therefore, cannot follow the flow reliably. This image also shows a lack of data in the center of the plume where the highest velocities are expected. This demonstrates the need for an improved velocimetry technique to capture the supersonic flow in the plume and better seeding methods. In Fig. 11b, the temperature profile of the SparkJet plume shows a maximum temperature of  $1600 \text{ K}$  after  $75 \mu\text{s}$ , which is consistent with CFD solutions of a similar configuration.<sup>22</sup>

### Force Stand Measurements

A miniaturized thrust stand was developed at APL under independent research and development sponsorship to assist with the characterization of various micropropulsion devices. The stand, pictured in Fig. 14a, consists of a small  $3 \times 3 \text{ cm}$  platform suspended by four rigid cantilever beams. A SparkJet actuator is bonded

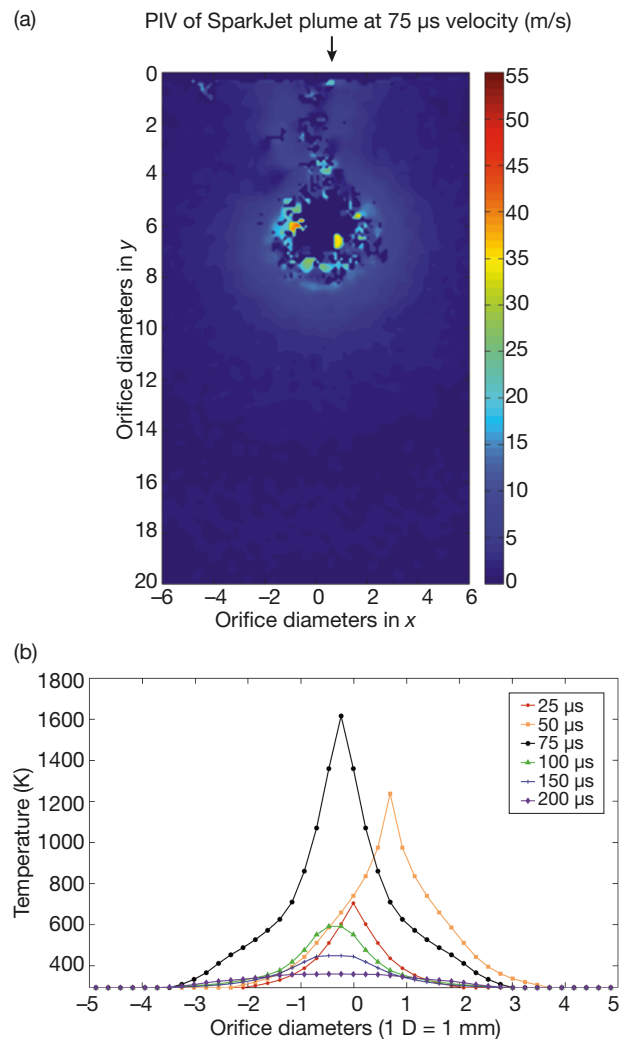


**Figure 13.** (a) Contour plot of the velocity magnitudes of the SparkJet plume using PIV and (b) the temperature profile of the plume at various time intervals at 1.85 mm above the SparkJet orifice. (Reproduced from Ref. 19 with permission of the American Institute of Aeronautics and Astronautics.)

directly to this movable 3 × 3 cm platform. Impulse imparted from the actuator causes the platform to vibrate ever so slightly. To measure the amplitude of these vibrations, a Michelson interferometer setup is used. The beam splitter shown in Fig. 14b then directs two beams, one stationary and one altered by the moving test stand, toward a photodiode detector where they generate an interference pattern. To minimize background vibrations due to environmental effects, the vacuum chamber and interferometer have been assembled on an optical bench with pneumatic isolation legs.

This miniature thrust stand was used to gather preliminary impulse bit data for a single SparkJet device. The SparkJet used for these tests was powered by a 220-nF capacitor rated at 1000 V. Impulse bit data were collected at five discrete voltage potentials ranging from 520

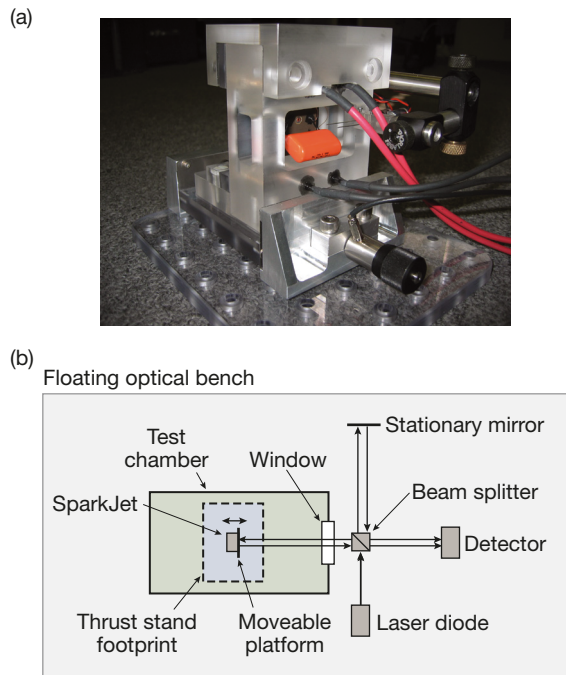


**Figure 14.** (a) APL miniature thrust stand. (b) Laser interferometer arrangement for measuring thrust stand vibrations. (Reproduced from Ref. 20 with permission of the American Institute of Aeronautics and Astronautics.)

to 900 V. These points correspond to energy deposition levels of 30, 40, 54, 70, and 89 mJ. A sample of these data is shown in Fig. 15. The impulse bit data appear to vary linearly with the deposited energy. The impulse bit data exhibit some scatter at each energy level. This could be due to inherent variation in the SparkJet performance or the measurement process itself. However, the general linearity of the curve suggests the performance of the SparkJet can be predicted within the range of deposited energy tested and possibly extrapolated to higher energy levels.

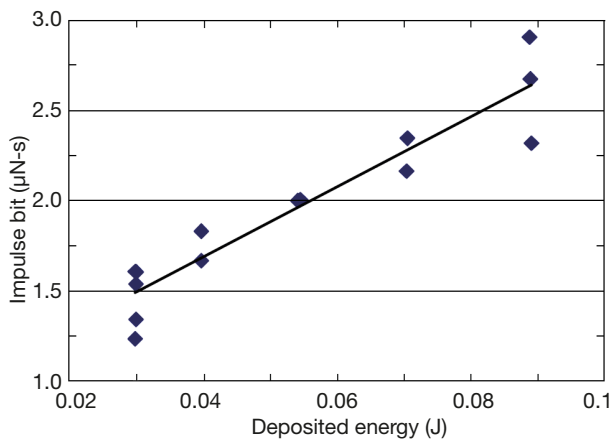


**Figure 15.** Preliminary SparkJet impulse bit measurements. (Reproduced from Ref. 20 with permission of the American Institute of Aeronautics and Astronautics.)

## Pressure Measurements

Previous experimental efforts have provided good agreement with CFD-based predictions for velocity and temperature distributions; however, these results did not provide a complete understanding of the SparkJet performance because of difficulty seeding the flow for PIV or difficulty obtaining consistent results for the DST. Therefore, attention was turned to measuring the pressure inside the SparkJet chamber.

The instantaneous pressure data were obtained using a PCB 105C22 dynamic pressure sensor (Fig. 16) installed in the bottom of the SparkJet cavity. The SparkJet assembly was designed such that the face of the pressure sensor is flush with the bottom of the cavity. This particular pressure sensor was chosen for its small size (2.5-mm sensing diameter), fast response time ( $<2 \mu\text{s}$ ), and high flash temperature tolerance. A significant benefit of using this sensor is the insensitivity to electromagnetic interference because shielding from electromagnetic interference emitting from the SparkJet circuitry and the spark itself has proven difficult in past experimental setups.

The time-dependent cavity pressure response was measured for a variety of configurations to determine the effects of cavity volume, orifice diameter, and initial stored capacitive energy. The initial blast wave from the arc discharge causes the sensor to resonate; therefore, the original pressure signal is then filtered using a fourth-order Butterworth filter to provide a cleaner signal for easier comparison with numerical results.

The PCB sensor sensing technology includes pre-loaded quartz crystals surrounded by the stainless steel housing. The loading on the quartz determines the output signal. In this experiment, both pressure changes and thermal expansion can affect the output signal because of the small size of the sensor and the proximity to the hot spark. To reduce the effects of the thermal shock associated with the initial blast wave, the exposed

face of the sensor is coated with black RTV and covered with 3M heavy duty electrical tape (0.25-mm thick). However, the long-term effects of the high-temperature air inside of the chamber expand the stainless steel housing and reduce the output signal such that the measured pressure signal is less than the actual chamber pressure. Therefore, only the filtered peak pressure value can be used to analyze a single spark event because the housing has not yet responded to the high-temperature air. This thermal expansion hypothesis has been supported on the basis of discussions with PCB technical engineers and a positive adjustment in the pressure signal when the sensor is more heavily thermally insulated. Future pressure cavity measurements will be made with a similar water-cooled PCB-made sensor with the hopes that the temperature effects on the sensor will be further reduced or eliminated.

As mentioned in the *Simplified Numerical Model* section, the energy stored in the capacitors is not completely transferred to heating the cavity air. Based only on the peak pressure, the SparkJet efficiency can be estimated by a comparison between experimental data and CFD results. CFD simulations were specifically tailored for comparison to these experimental efforts. The experimental SparkJet design parameters modeled by CFD include a cavity volume of  $44 \text{ mm}^3$ , orifice diameter of 1.0 mm, and capacitive input energy of 0.46 J. Shorter duration (500- $\mu\text{s}$ ) simulations focused on the initial pressure rise and were conducted over a range of energy deposition efficiencies. A separate boundary condition family was created at the base of the chamber that was the width of the pressure sensor used to measure cavity pressure. That boundary was then used to track the area-averaged pressure for the sensor versus time to compare with experimental data.

Figure 17 shows the pressure history assuming 20%, 35%, and 50% efficiencies using CFD. The peak pressure, based on experimental results, is very close



**Figure 16.** The PCB 105C22 dynamic pressure sensor.

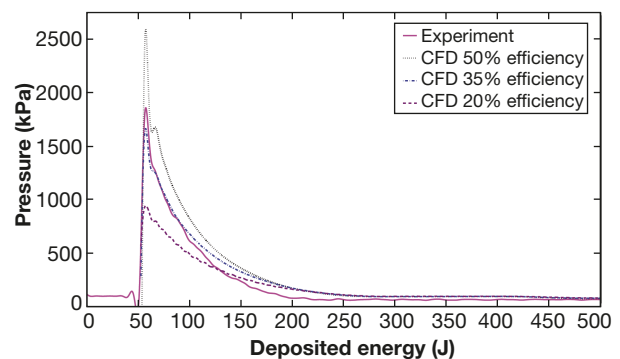


**Figure 17.** Comparison of a CFD simulated pressure signal and the resulting filtered experimental output signal using a fourth-order Butterworth filter. (Reproduced from Ref. 17 with permission of the American Institute of Aeronautics and Astronautics.)

to the 35% efficiency pressure curve, suggesting the SparkJet transfers 35% of the energy to heating the air in this configuration. Figure 17 also demonstrates the effect of the thermal expansion of the housing on the pressure signal, resulting in a more negative output. Beyond the first 50  $\mu\text{s}$  of Stage 2, the signal deviates from the 35% efficiency CFD prediction; this deviation is believed to be the result of thermal expansion of the sensor housing.

The efficiency of spark heat transfer to the air depends on the Joule heat produced by the spark. Joule heat is determined by the power drawn by the spark over the duration of the spark. The instantaneous power drawn by the spark is the product of voltage and current, which, according to Ohm's Law, is the product of the arc current squared and the resistance of the arc channel. For a capacitive spark discharge, the current ( $I$ ) across an arc is a function of the total storage capacitance and the voltage discharge rate of the capacitors. Therefore, to increase the power drawn by the spark while holding the input energy,  $Q$ , constant, the SparkJet design should maximize capacitance, resistance, and the capacitor discharge rate as demonstrated in Eq. 6:

$$W = IV = I^2 r = \left( C \frac{dV}{dt} \right)^2 r, \quad (6)$$

where  $W$  is electric power (J/s) and  $r$  is arc resistance (ohms).

Resistance across the arc gap is inversely proportional to the electric field strength ( $EF$ ) and is given by  $EF = V/d$ , where  $d$  is the electrode tip distance (in meters). Using this property and holding  $Q$  constant, the values of  $V$  and  $C$  can be adjusted such that a circuit with a large capacitance and low voltage potential will produce a more efficient spark than a circuit with a relatively smaller capacitance and a higher voltage potential. With a large capacitance and increased spark resistance due to the low

voltage potential, the discharge time of the capacitors is longer, thereby allowing more time for the spark to transfer heat to the air. In addition, simply increasing the gap distance between electrodes will increase arc resistance and, therefore, spark efficiency. However, the gap length is limited because if the gap resistance is too large, no spark will break down across the gap.

Figure 18 shows peak pressures for one physical SparkJet configuration with constant cavity volume ( $4.4 \times 10^{-8} \text{ m}^3$ ), orifice diameter (1 mm), and electrode gap width (1.75 mm) versus  $Q/E$ . Two separate power supplies configured the SparkJet: one power supply operated at 600 V of direct current with capacitance from 0.82 to 8.91  $\mu\text{F}$ , and the other power supply operated at 1000 V of direct current with capacitance from 0.22 to 2.47  $\mu\text{F}$ . The peak pressure data points corresponding to the power supply with the lower operating voltage and higher capacitance are represented by the black squares in Fig. 18. The peak pressure data points corresponding to the power supply with the higher operating voltage and lower capacitance are represented by the blue diamonds. For the same energy ratio values, the former power supply configuration provides peak pressures corresponding to 20% efficiency while the latter configuration more closely corresponds to 10% efficiency. This information will be extremely helpful when considering supporting electronics design.

### High-Frequency Actuation

The ability to actuate the SparkJet actuator over a wide frequency range (with sufficient momentum throughput) is required to meet the objective of upcoming wind-tunnel testing. This significant milestone was recently achieved in laboratory testing for all frequencies up to 1 kHz and for durations up to 1 s.

During benchtop testing, reliability (with 100% reliability meaning the SparkJet cycle occurs every time the trigger spark fires) was found to vary inversely with the spark gap resistance. However, based on earlier analysis of SparkJet efficiency, decreasing the spark gap distance decreases the heat transfer efficiency; therefore, there is a design trade-off between reliability and efficiency.<sup>26</sup>

### Preliminary Wind-Tunnel Testing

To demonstrate the effectiveness of the SparkJet actuator interacting with a supersonic boundary layer, an array of SparkJet actuators was installed in the FSU/Florida Center for Advanced Aero-Propulsion supersonic wind tunnel. The array included three SparkJet cavities with four 400- $\mu\text{m}$  orifices per cavity. Energy deposition in each cavity was achieved with a single pair of electrodes with a capacitance of approximately

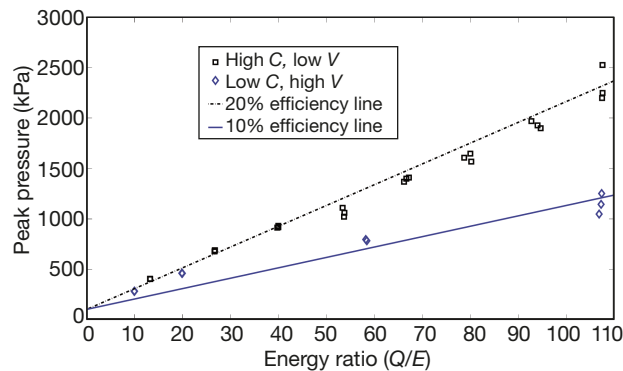


**Figure 18.** Peak pressure versus the SparkJet energy ratio powered by two different electrical setups but identical physical setups. (Reproduced from Ref. 17 with permission of the American Institute of Aeronautics and Astronautics.)

8  $\mu\text{F}$  per electrode pair. The SparkJet array was operated at very low frequency (0.2 Hz) to observe interaction during a single cycle and at high frequency (700 Hz) to determine whether high-frequency operation provided a stronger boundary layer interaction for the flat plate cross flow. Representing a second major milestone, this wind-tunnel testing at FSU/Florida Center for Advanced Aero-Propulsion (August 2011) provided evidence of successful, unsteady interaction between a supersonic (Mach 1.5) boundary layer and an array of SparkJet actuators.<sup>14</sup>

## CONCLUSIONS

The wide array of numerical and experimental efforts have provided a broad understanding of the SparkJet performance and the available design parameters for creating an effective SparkJet array in many challenging flow applications. This knowledge will be critical for accurately designing a SparkJet actuator array for upcoming application such as in open cavity flow and flow separation in low-pressure turbines. With the help of numerical modeling and numerous experimental techniques, our current understanding of a single SparkJet in quiescent flow is maturing. Our understanding of an array operating at a high frequency is just beginning; however, we assume most of the single SparkJet concepts will transfer to understanding the SparkJet array. This assumption was tested recently when the existing tools and databases created from this work were used to help design and deliver a SparkJet array for supersonic cavity flow testing at FSU.

## FUTURE WORK

A major milestone was met in mid-2011 when a SparkJet array underwent proof-of-concept testing in an FSU supersonic wind tunnel. Testing will be done to determine the influence of the SparkJet array on the shear layer associated with open cavity flow. The open cavity flow test will replicate the previous test except a SparkJet actuator array will replace the steady microjet array. The goal of this test is to show that the unsteadiness of the SparkJet arrays has a stronger effect on the cavity flow than that of steady jets. Beyond the supersonic testing, SparkJet arrays will be tested to control flow separation on turbine blades and in S-duct internal flows where high subsonic flows exist. Assuming the SparkJet arrays are effective in these flow fields, the SparkJet can be redesigned to offer control for a broad range of high-speed (and low-speed) flow applications.

**ACKNOWLEDGMENTS:** We acknowledge several people for their continued and critical support of this work:

H. Bruce Land III, Dave VanWie, Ashish Nedungadi, Jerry Emhoff, Joseph Katz (The Johns Hopkins University), and Jordan Wilkerson (formerly with APL). This material is based on research sponsored by AFOSR under consecutive research grants, the most recent being agreement FA-9550-09-1-0595. The U.S. government is authorized to reproduce and distribute reprints for governmental purposes notwithstanding any copyright notation thereon. The views and conclusions contained herein are those of the authors and should not be interpreted as necessarily representing the official policies or endorsements, either expressed or implied, of the AFOSR or the U.S. government.

## REFERENCES

- <sup>1</sup>Glezer, A., and Amitay, M., "Synthetic Jets," *Annu. Rev. Fluid Mech.* **34**(1), 503–529 (2002).
- <sup>2</sup>Corke, T. C., and Post, M. L., "Overview of Plasma Flow Control: Concepts, Optimization and Applications," in *Proc. 43rd AIAA Aerospace Sciences Meeting and Exhibit*, Reno, NV, paper AIAA-2005-563 (2005).
- <sup>3</sup>Diez-Garias, F., and Werner, D., "Microactuator Arrays for Sublayer Control in Turbulent Boundary Layers Using the Electrokinetic Principle," in *Proc. 38th AIAA Aerospace Sciences Meeting and Exhibit*, Reno, NV, paper AIAA-2000-0548 (2000).
- <sup>4</sup>Kral, L. D., "Active Flow Control Technology," ASME Fluids Engineering Division Technical Brief, ASME, New York (1998).
- <sup>5</sup>Kumar, V., and Alvi, F. S., "Efficient Control of Separation using Microjets," in *Proc. 35th AIAA Fluid Dynamics Conference and Exhibit*, Toronto, Ontario, paper AIAA-2005-4879 (2005).
- <sup>6</sup>Sahoo, D., Annaswamy, A., and Alvi, F., "Active Store Trajectory Control in Supersonic Cavities Using Microjets and Low-Order Modeling," *AIAA J.* **45**(3), 516–531 (2007).
- <sup>7</sup>Zhuang, N., Alvi, F., Alkislal, M., and Shih, C., "Supersonic Cavity Flows and Their Control," *AIAA J.* **44**(9), 2118–2128 (2006).
- <sup>8</sup>Ukeiley, L., Sheehan, M., Coiffet, F., Alvi, F., Arunajatesan, S., and Jansen, B., "Control of Pressure Loads in Geometrically Complex Cavities," *J. Aircr.* **45**(3), 1014–1024 (2008).
- <sup>9</sup>Land, H. B. III, Grossman, K. R., Cybyk, B. Z., and VanWie, D. M., "Solid State Supersonic Flow Actuator and Method of Use," U.S. Patent 7,988,103 (2 Aug 2011).
- <sup>10</sup>Hardy, P., Barricau, P., Caruana, D., Gleyzes, C., Belinger, A., and Cambonne, J., "Plasma Synthetic Jet for Flow Control," in *Proc. 40th Fluid Dynamics Conf. and Exhibit*, Chicago, IL, paper AIAA-2010-5103 (2010).
- <sup>11</sup>Narayananwamy, V., Raja, L., and Clemens, N., "Characterization of a High-Frequency Pulsed-Plasma Jet Actuator for Supersonic Flow Control," *AIAA J.* **48**(2), 297–305 (2010).
- <sup>12</sup>Shouman, K., Suplisson, A., Grove, J., and Bower, W., "Supersonic Store Separation at the Holloman High Speed Track," in *Proc. 53rd Society of Experimental Test Pilots Symp.*, Anaheim, CA (2009).
- <sup>13</sup>Cybyk, B. Z., and Wilkerson, J. T., "Performance Characteristics of the SparkJet Flow Control Actuator," in *Proc. 2nd AIAA Flow Control Conf.*, Portland, OR, paper AIAA-2004-2131 (2004).
- <sup>14</sup>Emerick, T., Ali, M., Foster, C., Alvi, F., Popkin, S., and Cybyk, B., "SparkJet Actuator Characterization in Supersonic Crossflow," *Proc. 6th Flow Control Conf.*, New Orleans, LA, paper AIAA 2012-2814 (2012).
- <sup>15</sup>Foster, C., Solomon, J., and Alvi, F., "Visual Study of Resonance Dominated Microjet Flows Using Laser-Based Micro-Schlieren," in *Proc. 49th AIAA Aerospace Sciences Meeting*, Orlando, FL, paper AIAA-2011-766 (2011).
- <sup>16</sup>Taylor, T., and Cybyk, B., "High-Fidelity Modeling of Micro-Scale Flow-Control Devices with Applications to the Macro-Scale Environment," in *Proc. 15th AIAA International Space Planes and Hypersonic Systems and Technologies Conf.*, Dayton, OH, paper AIAA-2008-2608 (2008).

- <sup>17</sup>Haack, S., Taylor, T., Emhoff, J., and Cybyk, B., "Development of an Analytical SparkJet Model," in *Proc. 5th Flow Control Conf.*, Chicago, IL, paper AIAA-2010-4979 (2010).
- <sup>18</sup>Haack, S., and Foster, C., "Experimental Estimation of SparkJet Efficiency," in *42nd AIAA Plasmadynamics and Lasers Conference*, Honolulu, HI, paper AIAA-2011-3997 (2011).
- <sup>19</sup>Haack, S., Land, H. B., Cybyk, B., Ko, H. S., and Katz, J., "Characterization of a High-Speed Flow Control Actuator Using Digital Speckle Tomography and PIV," in *Proc. 4th Flow Control Conf.*, Seattle, WA, paper AIAA-2008-3759 (2008).
- <sup>20</sup>Cybyk, B. Z., Simon, D. H., and Land, H. B. III, "Experimental Characterization of a Supersonic Flow Control Actuator," in *Proc. 44th AIAA Aerospace Sciences Meeting and Exhibit*, Reno, NV, paper AIAA-2006-478 (2006).
- <sup>21</sup>Bazelyan, E. M., and Raizer, Y. P., *Spark Discharge*, CRC Press, Boca Raton, FL (1998).
- <sup>22</sup>Cybyk, B. Z., and Grossman, K. R., "Single-Pulse Performance of the SparkJet Flow Control Actuator," in *Proc. 43rd AIAA Aerospace Sciences Meeting and Exhibit*, Reno, NV, paper AIAA-2005-401 (2005).
- <sup>23</sup>Roth, G., and Katz, J., "Five Techniques for Increasing the Speed and Accuracy of PIV Interrogation," *Meas. Sci. Technol.* **12**(3), 238–245 (2001).
- <sup>24</sup>Roth, G., Mascenik, D. T., and Katz, J., "Measurements of the Flow Structure and Turbulence Within a Ship Bow Wave," *Phys. Fluids* **11**(11), 3512–3523 (1999).
- <sup>25</sup>Sridhar, G., and Katz, J., "Drag and Lift Forces on Microscopic Bubbles Entrained by a Vortex," *Phys. Fluids* **7**(2), 389–399 (1995).
- <sup>26</sup>Popkin, S., Cybyk, B., Land, H., Foster, C., Emerick, T., and Alvi, F., "Recent Performance-Based Advances in SparkJet Actuator Design for Supersonic Flow Applications," in *Proc. 51st Aerospace Sciences Meeting*, Grapevine, TX, paper AIAA 2013-0322 (2013).

# The Authors

**Sarah H. Popkin** is a member of APL's Associate Professional Staff in the Aerospace Systems Design Group in the Force Projection Department. Ms. Popkin has conducted experimental testing since 2007 to measure SparkJet performance for a variety of designs and operating conditions. She also developed the simplified numerical model used to estimate SparkJet performance under high-frequency operation. **Trent M. Taylor** is a member of APL's Senior Professional Staff in the Aerospace Systems Design Group in the Force Projection Department. Dr. Taylor performed CFD analysis of the SparkJet for comparison to experimental testing. **Bohdan Z. Cybyk** is the Principal Investigator for this research grant. He is a member of APL's Principal Professional Staff and is Assistant Group Supervisor of the Aerospace Systems Design Group in the Force Projection Department. For this project, Dr. Cybyk provided overall project management, guided the research direction, and performed the CFD-based characterization studies of SparkJet operation in quiescent air and supersonic cross flow. For further information on the work reported here, contact Sarah Popkin. Her e-mail address is [sarah.popkin@jhuapl.edu](mailto:sarah.popkin@jhuapl.edu).